Physics of Plasmas ARTICLE pubs.aip.org/aip/pop

The dielectric response of plasmas with arbitrary gyrotropic velocity distributions

Cite as: Phys. Plasmas **32**, 092104 (2025); doi: 10.1063/5.0286477
Submitted: 19 June 2025 · Accepted: 25 August 2025 ·
Published Online: 5 September 2025

View Online Export Citation CrossMark

K. G. Klein[1,a] and D. Verscharen[2]

AFFILIATIONS

[1]Lunar and Planetary Laboratory, University of Arizona, Tucson, Arizona 85721, USA
[2]Mullard Space Science Laboratory, University College London, Dorking RH5 6NT, United Kingdom

[a]Author to whom correspondence should be addressed: kgklein@arizona.edu

ABSTRACT

Hot and tenuous plasmas are frequently far from local thermodynamic equilibrium, necessitating sophisticated methods for determining the associated plasma dielectric tensor and normal mode response. The Arbitrary Linear Plasma Solver is a numerical tool for calculating such responses of plasmas with arbitrary gyrotropic background velocity distribution functions (VDFs). To model weakly and moderately damped plasma waves accurately, we have updated the code to use an improved analytic continuation enabled by a polynomial basis representation. We demonstrate the continuity of solutions to the linear Vlasov–Maxwell dispersion relation between bi-Maxwellian and arbitrary VDF representations and evaluate the influence of VDF structure on mode polarization and wave power emission and absorption.

I. INTRODUCTION

Numerical solvers to the linear Vlasov–Maxwell dispersion relation have been extensively used to study the characteristics of linear plasma normal modes, in particular their growth or damping rates depending on plasma conditions.[1–5] However, typical linear plasma dispersion solvers assume a particular analytical form for the underlying background velocity distribution function (VDF) $f_{0,s}(v)$, e.g., a bi-Maxwellian (WHAMP,[6] PLUME,[7] NHDS,[8] or BO[9]) or a bi-κ (DSHARK[10]) distribution. Such an assumption enables the determination of the linear dispersion relation through the evaluation of a closed equation in terms of known special functions that simplify the required integrals over velocity space. However, many space and astrophysical plasmas, and collisionless plasmas generally, are not well represented by bi-Maxwellian, or even bi-κ, distributions. The plasma systems can be in a state far from local thermodynamic equilibrium, cf. reviews by Marsch[11] and Verscharen *et al.*[12] These departures require a more sophisticated treatment of the dispersion relation.

The Arbitrary Linear Plasma Solver (ALPS) is an Message Passing Interface (MPI) parallelized numerical code written in FORTRAN90 that solves the Vlasov–Maxwell dispersion relation for a hot, magnetized plasma.[13] ALPS allows for any number of particle species with arbitrary gyrotropic background distribution functions supporting normal modes with any direction of propagation with respect to the background magnetic field, and can include the effects of special relativity in the dielectric plasma response.

Instead of using parameterized values for a collection of analytical functions, ALPS uses as input the phase-space density on a discrete grid of parallel and perpendicular momentum $f_{0,s}(p_\perp, p_\parallel)$, which in the non-relativistic case is directly equivalent to a velocity grid $f_{0,s}(v_\perp, v_\parallel)$. ALPS evaluates the dispersion relation through a direct numerical integration of the gradients and other functions of $f_{0,s}$; see Eqs. (2.9) and (2.10) of Verscharen *et al.*[14] This method has been applied to spacecraft data from both MMS[15–17] and Wind,[18] showing significant deviations of wave behavior from predictions calculated using simple analytical functions. It has been applied to the study of a variety of kinetic numerical simulations with significant departures from Maxwellian VDFs.[19–21]

The initial ALPS implementation is described by Verscharen *et al.*[14] Recent additions to the code include the calculation of the associated eigenfunctions and a partitioning of the species heating rates into the component mechanisms, e.g., Landau, Transit Time, and Cyclotron damping, as well as the option to treat selected plasma components as bi-Maxwellians for numerical expediency. These changes are discussed in Sec. II. The original code struggled with the evaluation of the Landau contour integral essential for characterizing damped solutions for some VDFs with strong non-Maxwellian features. We present updates that enable a more accurate representation in this

evaluation for moderately damped solutions for such VDFs. We explore the impact of the updated representation on weakly and moderately damped modes in Sec. III. We demonstrate the continuity of solutions between bi-Maxwellian fits and the ALPS direct calculation, as well as the changes for the underlying eigenfunctions and damping rates, in Sec. IV. Details of the underlying numerics are found in Appendixes A, B, and C.

II. DISPERSION RELATIONS FOR ARBITRARY DISTRIBUTIONS

ALPS allows for the inclusion of any number of particle species or components with arbitrary gyrotropic background distributions $f_{0,s}(p_\perp, p_\parallel)$ as a function of momentum $\mathbf{p}$, supporting normal modes with any direction of propagation, represented by the wavevector $\boldsymbol{k} = \boldsymbol{k}_\perp + \boldsymbol{k}_\parallel$. Throughout this text, $\perp$ and $\parallel$ are defined with respect to the direction of the background magnetic field $\boldsymbol{B}_0$.

Vlasov–Maxwell theory starts with the expression for the first-order perturbation of the current

$$\mathbf{j} = \sum_s \mathbf{j}_s = \sum_s q_s \int d^3\mathbf{p}\, \mathbf{v}\delta f_s(\mathbf{r}, \mathbf{p}, t) = -\frac{i\omega}{4\pi}\underline{\underline{\chi}}_s \cdot \mathbf{E}, \tag{1}$$

where q_s is the charge of a particle of species s, ω is the complex wave frequency with real and imaginary components ω_r and γ, $\mathbf{E}$ is the electric field, $\underline{\underline{\chi}}_s$ is the susceptibility of species s, and δf_s is the fluctuation of the VDF from the background $f_{0,s}$. Following the careful application of identities, transformations, and substitutions outlined by Verscharen *et al.*[14] and covered in detail in Chap. 10 of Stix,[22] we arrive at an expression for $\underline{\underline{\chi}}_s$ in terms of integrals over functions of momentum derivatives of the background VDF

$$\underline{\underline{\chi}}_s = \frac{\omega_{p,s}^2}{\omega\Omega_{0,s}} \int_0^\infty 2\pi p_\perp dp_\perp \int_{-\infty}^\infty dp_\parallel \left[\hat{e}_\parallel \hat{e}_\parallel \frac{\Omega_s}{\omega} p_\parallel^2 \times \left(\frac{1}{p_\parallel}\frac{\partial f_{s,0}}{\partial p_\parallel} - \frac{1}{p_\perp}\frac{\partial f_{s,0}}{\partial p_\perp}\right) + \sum_{n=-\infty}^{\infty} \frac{\Omega_s p_\perp U}{\omega - k_\parallel v_\parallel - n\Omega_s} \underline{\underline{T}}_n\right], \tag{2}$$

where

$$U = \frac{\partial f_{0,s}}{\partial p_\perp} + \frac{k_\parallel}{\omega}\left(v_\perp \frac{\partial f_{0,s}}{\partial p_\parallel} - v_\parallel \frac{\partial f_{0,s}}{\partial p_\perp}\right), \tag{3}$$

$$\underline{\underline{T}}_n = \begin{pmatrix} \frac{n^2 J_n^2}{z^2} & \frac{inJ_nJ_n'}{z} & \frac{nJ_n^2 p_\parallel}{zp_\perp} \\ -\frac{inJ_nJ_n'}{z} & (J_n')^2 & \frac{-iJ_nJ_n'p_\parallel}{p_\perp} \\ \frac{nJ_n^2 p_\parallel}{zp_\perp} & \frac{iJ_nJ_n'p_\parallel}{p_\perp} & \frac{J_n^2 p_\parallel^2}{p_\perp^2} \end{pmatrix}, \tag{4}$$

and J_n is the nth order Bessel function with argument $z = k_\perp v_\perp/\Omega_s$ and J_n' is its derivative. Characteristic timescales are defined in terms of the plasma frequency $\omega_{ps} = \sqrt{4\pi n_s q_s^2/m_j}$ and the (signed) cyclotron frequency $\Omega_s = q_s B_0/m_s c$; $\Omega_{0,s}$ only includes the rest-mass in the denominator, while Ω_s includes the appropriate relativistic correction.

As described in Appendix A, ALPS may now use $\underline{\underline{\chi}}_j$ from the bi-Maxwellian approximation as determined by NHDS[8] or the cold plasma expression for any of the species' contribution to the dispersion relation. This capability is useful when one of the components is well modeled as a fluid or the velocity distribution is not constrained by observations.

ALPS has also been updated so that the user may specify any analytic form for $f_{0,s}(p_\perp, p_\parallel)$, allowing the direct calculation of the appropriate derivatives and integrals through quadrature on a specified grid, as well as the immediate extension to complex $p_\parallel$ values without the need for any fitting or polynomial representations during the evaluation of the analytic continuation. While not applicable to cases where a simulation or model is not easily expressible in analytical form, it can be particularly useful when a theory predicts an analytical, but non-Maxwellian or non-κ form (e.g., a bi-Moyal flattop distribution[23]) so that differences against standard bi-Maxwellian predictions can be quantified.

For the non-analytical contributions, ALPS calculates $\partial f_{0,s}/\partial p_\parallel$ and $\partial f_{0,s}/\partial p_\perp$ on the prescribed grid and performs the necessary integrations, allowing the construction of the dielectric tensor

$$\underline{\underline{\varepsilon}}(\omega, \mathbf{k}) = \underline{\underline{1}} + \sum_s \underline{\underline{\chi}}_s(\omega, \mathbf{k}), \tag{5}$$

which in turn allows the construction of the homogeneous linear wave equation

$$\underline{\underline{\Lambda}} \cdot \mathbf{E} = \begin{pmatrix} \varepsilon_{xx} - n_z^2 & \varepsilon_{xy} & \varepsilon_{xz} + n_x n_z \\ \varepsilon_{yx} & \varepsilon_{yy} - n_x^2 - n_z^2 & \varepsilon_{yz} \\ \varepsilon_{zx} + n_x n_z & \varepsilon_{zy} & \varepsilon_{zz} - n_x^2 \end{pmatrix} \begin{pmatrix} E_x \\ E_y \\ E_z \end{pmatrix} = 0, \tag{6}$$

where $\boldsymbol{n} = c\mathbf{k}/\omega$ is the complex index of refraction. The solutions of $\Lambda = \det|\underline{\underline{\Lambda}}(\omega, \mathbf{k})| = 0$ are the normal modes supported by the prescribed background. ALPS identifies these solutions for fixed wavevectors as minima over a user-defined region of complex frequency space and follows identified solutions as a function of varying wavevector $\mathbf{k}d_{\mathrm{ref}}$, where $d_{\mathrm{ref}} = c/\omega_{p,\mathrm{ref}}$ is the reference inertial length. In addition to determining dispersion relations, ALPS also calculates the associated eigenfunctions of the fluctuating electromagnetic fields, densities, and velocities. These eigenfunctions represent the polarization of the identified plasma normal modes. ALPS also calculates the damping or growth rates associated with each species, and further separates the contributions to these rates from Landau, transit time, and cyclotron mechanisms. The details of the eigenfunction and heating calculations are included in Appendix B.

III. IMPROVED HYBRID ANALYTIC CONTINUATION

When the solutions are damped [$\gamma < 0$, where $\gamma = \mathbb{I}\mathrm{m}(\omega)$] the integration of Eq. (2) necessitates an analytic continuation of $f_{0,s}$ into the complex $p_\parallel$ plane. This is straightforward if $f_{0,s}$ is a known analytical function which can be evaluated at a complex $p_\parallel$.[24] For the non-analytical case, as we only have values for $f_{0,s}$ for $\mathbf{p} \in \mathbb{R}$, we use two complementary schemes to extend the distribution function numerically. The initial implementation of ALPS is a fit of $f_{0,s}$ to a (typically small) number of analytical functions, Sec. III A. In this work, we describe a newly implemented polynomial basis representation using a generalized linear least squares approach, Sec. III B. In both cases, we follow the prescription in Landau[25] for the integration of a function G over a contour C_L that lies below the complex poles of the integrand

$$I(p_\perp) = \int_{C_L} \mathrm{d}p_\parallel G(p_\perp, p_\parallel) = \begin{cases} \int_{-\infty}^{+\infty} \mathrm{d}p_\parallel G(p_\perp, p_\parallel) & \text{if } \gamma > 0, \\ \mathscr{P}\int_{-\infty}^{+\infty} \mathrm{d}p_\parallel G(p_\perp, p_\parallel) + i\pi \sum \mathrm{Res}_A(G) & \text{if } \gamma = 0, \\ \int_{-\infty}^{+\infty} \mathrm{d}p_\parallel G(p_\perp, p_\parallel) + 2i\pi \sum \mathrm{Res}_A(G) & \text{if } \gamma < 0, \end{cases} \quad (7)$$

where $\mathscr{P}$ indicates the principal-value integration, $\mathrm{Res}_A(G)$ is the residue of the function G at point A, and the sum is taken over all poles A. For the integral of interest in Eq. (2), G has one simple pole with

$$\sum \mathrm{Res}_A(G) = -\frac{m_j}{|k_\parallel|}\Omega_j U \underline{\underline{T}}_n\Big|_{p_\parallel = p_{\mathrm{pole}}}, \quad (8)$$

which has to be evaluated for the six unique terms in $\underline{\underline{T}}_n$.

In the non-relativistic instance of the code, ALPS evaluates the fit or representation separately at each value of $p_\perp$ on the grid, so that no assumption is made as to the structure of $f_{0,s}$ in the $p_\perp$-direction. ALPS uses these functions only if a pole is within the integration domain—the momentum range provided in the input VDF grid—and only if $\gamma \leq 0$. Therefore, the method of analytic continuation does not impact purely unstable solutions.

A. Fit function representation

In the original version of ALPS, to calculate the analytic continuation, the user specifies a small number of analytical functions (usually one or two, corresponding to core-and-beam structures inferred from *in situ* solar wind observations[11,26]) each with a handful of defining parameters. The canonical case used is a linear combination of drifting bi-Maxwellians,

$$f_{0,s} = \frac{1}{\pi^{3/2} m_s^3 w_{\perp s}^2 w_{\parallel s}} \exp\left(-\frac{p_\perp^2}{m_s^2 w_{\perp s}^2} - \frac{(p_\parallel - m_s U_s)^2}{m_s^2 w_{\parallel s}^2} \right), \quad (9)$$

but bi-κ,

$$f_{0,s} = \frac{1}{m_s^3 w_{\perp s}^2 w_{\parallel s}} \left[\frac{2}{\pi(2\kappa - 3)}\right]^{3/2} \frac{\Gamma(\kappa + 1)}{\Gamma(\kappa - 1/2)} \times \left\{ 1 + \frac{2}{2\kappa - 3}\left[\frac{p_\perp^2}{m_s^2 w_{\perp s}^2} + \frac{(p_\parallel - m_s U_s)^2}{m_s^2 w_{\parallel s}^2} \right] \right\}^{-(\kappa+1)}, \quad (10)$$

where Γ is the Gamma function, and Jüttner distributions,

$$f_{0,s} = \frac{1}{2\pi m_s^3 c w_s^2 K_2(2c^2/w_s^2)} \exp\left(-2\frac{c^2}{w_s^2}\sqrt{1 + \frac{|p|^2}{m_s^2 c^2}} \right), \quad (11)$$

are included. Additional functions, including two other representations of the Jüttner distribution as well as a bi-Moyal distribution,

$$f_{0,s} = A \exp\left\{ \frac{1}{2}\left[\frac{p_\perp^2}{m_s^2 w_{\perp s}^2} + \frac{(p_\parallel - m_s U_s)^2}{m_s^2 w_{\parallel s}^2} - \exp\left(\frac{p_\perp^2}{m_s^2 w_{\perp s}^2} + \frac{(p_\parallel - m_s U_s)^2}{m_s^2 w_{\parallel s}^2} \right) \right] \right\}, \quad (12)$$

with A as normalization constant, have been added since the initial code release.

At each $p_\perp$ value, a 1-D Levenberg–Marquardt fit[27,28] is performed as a function of $p_\parallel$. For $p_\perp = 0$, user-defined inputs are used to initialize the fit parameters. ALPS uses the final fit results from $p_\perp = 0$ as the initial guess for the next $p_\perp$ value, eventually iterating across the entire $p_\perp$ range. This process works well for sufficiently smooth functions and fit initializations sufficiently close to a minimum for the Levenberg–Marquardt algorithm.

However, when applying the code to more complicated VDFs, two recurrent difficulties can arise that necessitate the development of a new representation method. First, even when a good set of fit initializations was selected, the fitting routine could fail at larger $p_\perp$ values, typically due to pathological but not unphysical variations of the VDF as a function of $p_\perp$, e.g., the disappearance of a secondary population or the appearance of an additional population at larger $p_\perp$. This failure would cause the entire fitting procedure to halt. Second, even when the fits converge for all $p_\perp$, the small number of functions used for the analytical representation leads to inaccuracies in the representation of the VDF, producing discrepancies as dispersion relations cross from $\gamma > 0$ to $\gamma < 0$ or vice versa.

These discrepancies arise for two reasons. First, the momentum derivatives of $f_{0,s}$ and the fit function can differ when evaluated at the resonant velocity $v_{\mathrm{res}} = (\omega - n\Omega_s)/k_\parallel$. Second, the total velocity moments of the fit function can differ from the velocity moments of the actual VDF, leading to an effective net charge and current that is different for $\gamma > 0$ and $\gamma < 0$. In addition to producing incorrect mode structure for damped solutions, these discrepancies can lead to a sharp edge at $\gamma = 0$ that causes the numerical Newton-secant search used to follow dispersion relations with varying wavevector to jump to a different solution or lose the physical solutions entirely due to the large unphysical gradient in Λ. Such a jump is illustrated in the surfaces associated with low-order fits in Fig. 1, e.g., the gray line in the lower right panel.

These issues with the fit function representation for VDFs that are significantly different from a finite superposition of Maxwellian functions in the $p_\parallel$ dimension have led us to the development of a new approach to perform the hybrid analytic continuation, combining numerical integration of the input VDF with a *polynomial basis representation* when the dispersion relation requires evaluation of the VDF at complex momentum values.

B. Polynomial basis representation

To reduce the discrepancies associated with representing $f_{0,s}$ using one or a handful of physically representative fitted analytical functions, we have implemented a Generalized Linear Least Squares (GLLS) representation of $f_{0,s}(p_\parallel)$ for fixed values of $p_\perp$, following Sec. 15.4 of Press *et al.*[29] Specifically, we find the parameters a_k for the model

$$y(x) = \sum_{k=0}^{M-1} a_k X_k(x), \quad (13)$$

where $X_k(x)$ are a set of basis functions and $y(x)$ is the data to be fit. For this implementation, we have selected the Chebyshev polynomials $T_k(x)$ of the first kind as the basis functions, which are defined recursively through

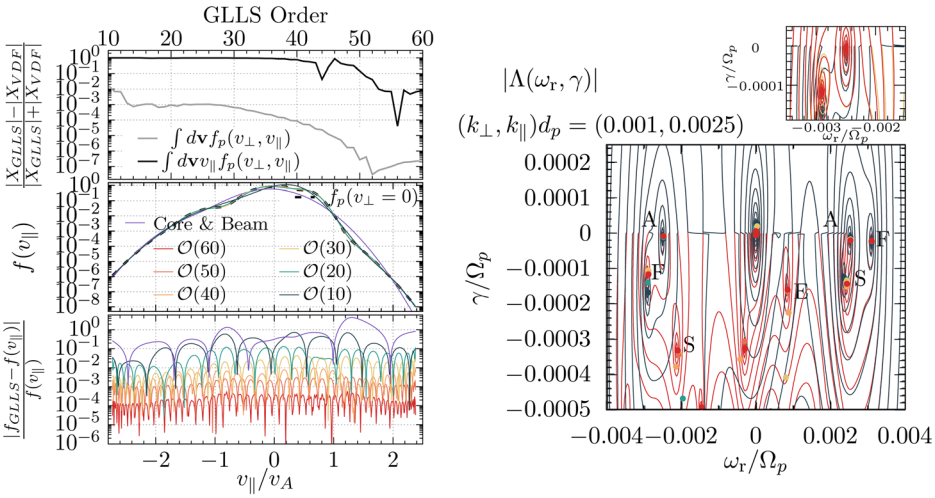

FIG. 1. (Left) Comparison of input $f_{0,p}(v_\perp = 0, v_\parallel)$ with GLLS Chebyshev representations and a fit consisting of the sum over two bi-Maxwellians. (Top) Relative percentage difference in the density (gray) and current (black) between the GLLS and input VDFs as functions of the GLLS order. The middle and bottom panels show the reconstructed $f_{0,p}$ at $v_\perp = 0$ as well as the relative error compared to the input VDF. (Right) Isocontours of constant $\Lambda(\omega_r, \gamma)$ for ALPS solutions using the GLLS analytic continuation for O(10) (gray dashed) and O(60) (red), using $(k_\perp, k_\parallel)d_p = (0.001, 0.0025)$. The above inset illustrates the transition between the extreme orders used in this work over a limited region of complex frequency space. Identified solutions with $\Lambda = 0$ are shown with colored dots using the same color scale as the left panels, with letters indicating Slow, Alfvén, Fast, or Entropy mode (SAFE) solutions.

$$T_0(x) = 1, \tag{14}$$

$$T_1(x) = x, \tag{15}$$

$$T_{n+1}(x) = 2xT_n(x) - T_{n-1}(x). \tag{16}$$

As T_n are bound between $[-1, 1]$, we perform a change of variables from $p_\parallel$ to x through

$$x = \frac{p_\parallel - \left(p_\parallel^{\max} + p_\parallel^{\min}\right)/2}{\left(p_\parallel^{\max} - p_\parallel^{\min}\right)/2}, \tag{17}$$

where $p_\parallel^{\max,\min}$ are the maximum and minimum values of the input VDF grid.

The bounded nature of T_n is ideally suited to the limited range of $p_\parallel$ used as inputs for ALPS. Chebyshev polynomial representation performs better than other classes of orthogonal polynomials, e.g., the Hermite or Legendre polynomials, not shown. We model $\log_{10}[f_{0,s}]$ rather than $f_{0,s}$ to capture the full range of the VDF amplitude and not solely the structure near the peak of the distribution. We emphasize that, as with the functional fitting approach discussed in Sec. III A, this is a purely one-dimensional method, representing $f_{0,s}(p_\parallel)$ separately for the $n_\perp$ rows in the input VDF grid; we write the VDF slice that we represent as y_i, which is known at N values of x.

The solution is performed via the normal equations method, solving

$$\sum_{j=0}^{M-1} \alpha_{kj} a_j = \beta_k, \tag{18}$$

where

$$\alpha_{kj} = \sum_{i=0}^{N-1} \frac{X_j(x_i) X_k(x_i)}{\sigma_i^2}, \tag{19}$$

and

$$\beta_k = \sum_{i=0}^{N-1} \frac{y_i X_k(x_i)}{\sigma_i^2}. \tag{20}$$

If the errors in the knowledge of y_i are known, one can set σ_i to nonunity values; in the current implementation, $\sigma_i = 1 \forall x_i$. Equation (18) is solved using the dgemm, dgemv, and dgesv routines from the LAPACK library. As the GLLS solution is calculated once for an input VDF, there is no need to implement more efficient existing schemes for determining a_{kj} that exploit connections between Fourier and Chebyshev representations (e.g., Ref. 30).

The polynomial basis method produces superior results compared to the functional fitting method for highly structured VDFs, both in terms of the smoothness of $\Lambda(\omega)$ across $\gamma = 0$ due to improved accuracy of $\partial_p f_{0,j}$ for all ω and $\mathbf{k}$ values, as well as in correctly capturing the total density and current of the VDFs. To illustrate this, Fig. 1 shows the representation of a slice of $f_{0,p}(p_\parallel)$ for $p_\perp = 0$ using the GLLS method for orders $N = (10, 20, 30, 40, 50, 60)$ and the best fit to the sum of two bi-Maxwellians. Also shown are the relative differences between the fit or GLLS representation and the actual VDF slide. We consider a distribution similar to one from Walters *et al.*,[18] interpolated from Wind Solar Wind Experiment (SWE) observations to a fixed grid of 300 × 600 points in $(p_\perp \times p_\parallel)$. Looking at the $p_\perp = 0$ slice, neither the bi-Maxwellian fit (purple) nor the lowest order GLLS representation (gray) of $f_p(p_\parallel)$ match the actual distribution, with the relative error approaching or exceeding order unity. Moving to higher order representations, the relative error decreases by several orders of magnitude; the highest order we consider, O(60), is well below the number of resolved points in $p_\parallel$, ensuring we are not over-fitting the distribution.

In the right-hand panels of Fig. 1, we plot isocontours of the magnitude of $\log_{10}[\Lambda(\omega_r, \gamma)]$, as well as the associated solutions satisfying

$\Lambda = 0$, for a wavevector of $(k_\perp, k_\parallel)d_p = (0.001, 0.0025)$. The isocontours for both the lowest, O(10), and highest, O(60), representations are shown. For the O(10) case (gray dashed lines), there is a stark discontinuity across $\gamma = 0$, indicating that the VDF representation is not sufficiently accurate in its representation of the bulk velocity moments and resonant momentum gradients involved in the principal-value integration, Eq. (7), to enable a smooth transition between growing and damping solutions. For the O(60) case (red), the isocontours are continuous across $\gamma = 0$; the transition between these two orders over a limited region of complex frequency is illustrated in the upper right inset, illustrating the convergence toward a smooth surface with higher polynomial order.

In addition to the $\gamma = 0$ discontinuity, the damping rates of the moderately damped modes are significantly altered depending on the order of the GLLS representation. The backward-propagating Fast solution—with the sign of ω_r indicating the direction of propagation—becomes significantly less damped with increasing order, while the forward-propagating slow solution becomes more damped. We see the complex frequencies of the moderately damped solutions begin to converge at O(50), which defines the order that we use for the remainder of this work.

In considering a wider set of test VDFs, we find that the error in the density (zeroth velocity moment of $f_{0,s}$) and background current (first velocity moment of $f_{0,s}$) of the reconstructed VDF serves as a good proxy for deciding whether the reconstruction order is sufficiently high for our hybrid analytic continuation method to work. The relative error between the representation and the input VDFs is shown for both quantities as a function of order in the top panel of Fig. 1. We see that good agreement can be achieved with relatively low order for the density, but that higher orders are needed to reduce the error in the current. We find that a relative percent difference[31] $|X_{GLLS} - X_{VDF}|/|X_{GLLS} + X_{VDF}|$ of less than 0.1 is typically sufficient for the method to yield reliable results.

While a relative error of the current of less than 10% is generally sufficient for the solutions to converge, for the case of more pathological VDFs, additional convergence studies should be considered. An example convergence study for the same VDF as used in Fig. 1 is shown in Fig. 2 for the forward-propagating Alfvén solution varying $k_\parallel d_p$ for fixed $k_\perp d_p = 0.001$. Both the real and imaginary parts of the complex frequency ω are shown, alongside the relative error compared to the solution based on GLLS of order O(60). We see that ω_r is largely unaffected until significant damping arises, at which point the differences in the damping rates change the speed of propagation of the modes. The growth rates $\gamma > 0$ are correct for all orders as expected due to the analytic continuation not being invoked for these solutions according to Eq. (7). The damped modes have 5%–10% differences for the low-order solutions compared to the converged solution. Moreover, when transitioning across $\gamma = 0$, the lower order representations can jump to unphysical solutions. The impact of representations with unnecessarily high order on strongly damped solutions is discussed in Appendix C.

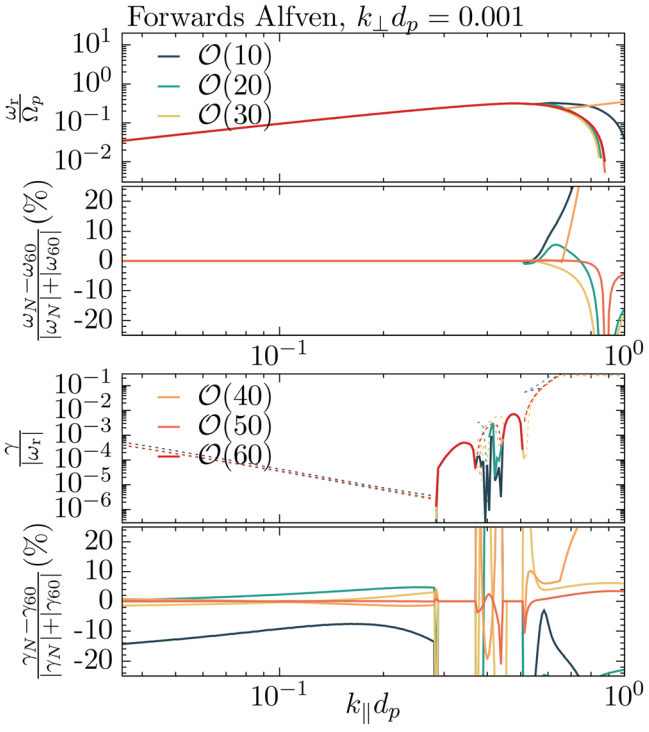

FIG. 2. Real and imaginary parts of the complex frequency $\omega = \omega_r + i\gamma$ for the parallel propagating Alfvén/ion cyclotron wave using GLLS representations with $\mathcal{O}(10)$ through $\mathcal{O}(60)$. The relative error between the lower-order and $\mathcal{O}(60)$ solutions illustrates the order necessary for convergence for the input VDF.

IV. COMPARING DISPERSION RELATIONS

A. Validating against bi-Maxwellian models

We next turn to the consideration of the relation between the ALPS solutions and those calculated based on multi-component

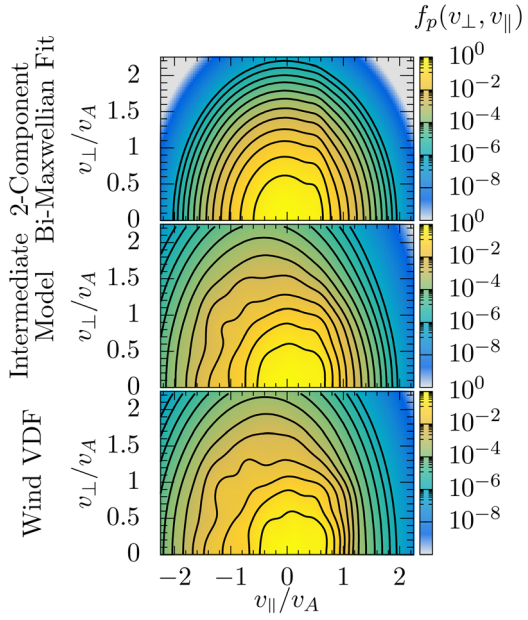

FIG. 3. Input proton VDFs used for the ALPS calculations, including the best-fit two-bi-Maxwellian $f_{C\&B}$ (top), observed wind VDF $f_{Obs.}$ (bottom), and one intermediate model, Eq. (25) (middle).

bi-Maxwellian fits to the background VDF. To investigate this, we consider the same observed proton VDF measured by the Wind spacecraft of the solar wind interval considered in Sec. III—$f_{Obs}(v_\perp, v_\parallel)$—as well as a two-component bi-Maxwellian best fit of the proton VDF, $f_{C\&B}(v_\perp, v_\parallel)$ imposed on a discrete velocity grid. These VDFs are shown in the top and bottom panels of Fig. 3.[32] We use these two input VDFs to calculate the associated linear dispersion relations, shown in Fig. 4 for both the backwards and forwards parallel-propagating Alfvén solutions; $k_\perp d_p$ is fixed at 0.001. Both VDFs have the same velocity resolution, and the ALPS bi-Maxwellian solution agrees with a "traditional" calculation from PLUME (not shown). As previously noted by Walters *et al.*,[18] the real parts of the frequency ω_r/Ω_p for the solutions based on f_{Obs} and $f_{C\&B}$ are qualitatively the same at large scales, deviating only when the damping is sufficiently strong to slow the propagation of the wave. For clarity, we only plot solutions for which $|\gamma|/|\omega_r| < 1/e$, indicating they are not too strongly damped.

The wavevector regions of instability are significantly different when using f_{Obs} or $f_{C\&B}$. The forward Alfvén mode is stable for the core-and-beam VDF, but supports two regions of instability, with the smaller scale region having a moderate growth rate. Both backwards Alfvén modes support instabilities, but the observed VDF is more unstable, with a broad range of unstable wavevectors.

The perpendicular electric field polarization of the solutions[33]

$$\mathscr{P}_{xy} = \frac{|E_R| - |E_L|}{|E_R| + |E_L|} \ni E_{R,L} \equiv \frac{E_x \mp i E_y}{\sqrt{2}}, \tag{21}$$

as well as the resonant velocities

$$v_\parallel^{\text{res}} = \frac{\omega - n\Omega_p}{k_\parallel}, \tag{22}$$

where the left-handed waves (forward Alfvén and backward fast) have $n = 1$ and the right-handed waves (backwards Alfvén and forward fast) have $n = -1$, are effectively identical between the solutions from the two models.

What drives these differences can be identified using quasilinear theory.[33,34] The resonant coupling of the wave to the VDF can be represented in terms of the operator

$$\mathscr{G} \equiv \left(1 - \frac{k_\parallel v_\parallel}{\omega_r}\right)\frac{\partial}{\partial v_\perp} + \frac{k_\parallel v_\perp}{\omega_r}\frac{\partial}{\partial v_\parallel}, \tag{23}$$

applied to $f_p(v_\perp, v_\parallel)$. To illustrate the structures of the VDF responsible for growth and damping, we construct a $k_\parallel$-dependent function, applying $\mathscr{G}$ to f_p at $v_\perp$ and the resonant parallel velocity associated with each wavevector,

$$\mathscr{G}\left[f_p\left(\frac{v_\parallel^{\text{res}}(k_\parallel d_p)}{v_A}, \frac{v_\perp}{v_A}\right)\right] \ni \frac{v_\parallel^{\text{res}}(k_\parallel d_p)}{v_A} = \frac{\omega_r/\Omega_p - n}{k_\parallel d_p}. \tag{24}$$

Velocities are normalized to the Alfvén velocity $v_A = B/\sqrt{4\pi n_p m_p}$. This function is illustrated in the bottom two rows of Fig. 4. As this calculation is only valid in the weak damping or growth limit[34] $|\gamma|/|\omega_r| < 1/e$, and only useful when the resonant velocity samples the input VDF, we restrict ourselves to the limited range of wavevectors satisfying both these conditions. The sign of this function at each velocity value indicates whether that point in phase space emits or absorbs power in interaction with the given wave. As illustrated by

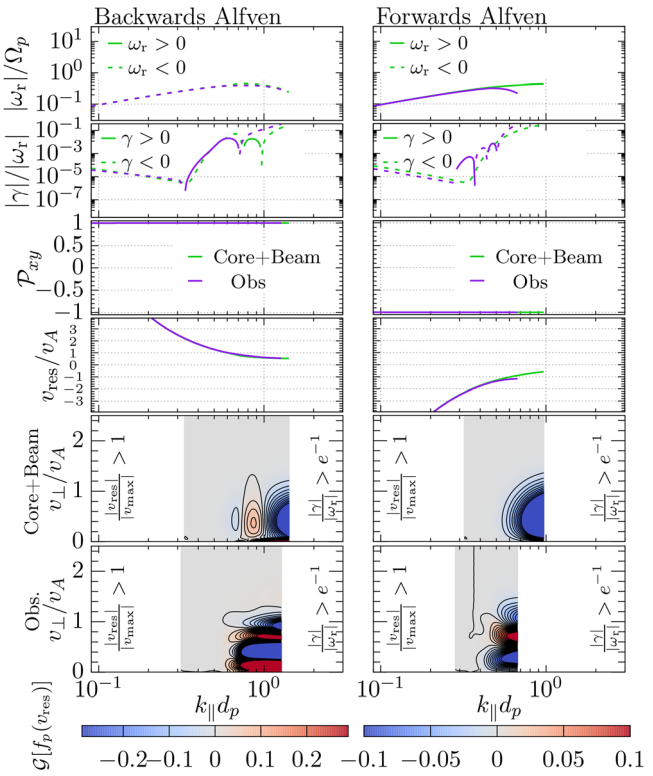

FIG. 4. Dispersion relations for parallel-propagating Alfvén waves supported by the observed (green lines) and core-and-beam (purple) VDFs: (top row) real part of the frequency ω_r/Ω_p (second) growth (solid) and damping (dashed) rates per wave period γ/ω_r (third) polarization P_{xy}, and (fourth) resonant velocity v_{res}/v_A. The bottom two rows show the quasilinear operator applied to the resonant velocity associated with wavevector, $G\left\{f_p[v_\parallel^{res}(k_\parallel d_p)]\right\}$ from Eq. (24). The structure in this space illustrates the velocity regions responsible for wave emission (red) and absorption (blue).

Walters *et al.*,[18] the sign of the function integrated over $v_\perp$ indicates whether the species has a net absorption or emission at that parallel scale.

For the forward Alfvén solution, there is no portion of the core-and-beam VDF that drives an instability. For the observed VDF, structures at $v_\parallel \sim -v_A$ and $v_\perp \in [0.5, 1]v_A$ are responsible for the range of strongly unstable modes; isocontours of the VDFs are shown in the left-hand column of Fig. 7. For the backwards Alfvén waves, the structure responsible for emission is starkly different between the two VDF representations, with all $v_\perp$ values coherently contributing to the core-and-beam emission over a narrow band of $v_\parallel$ values. The observed VDF has a striated structure in $v_\perp$ with different velocity regions competing to enhance or reduce the wave emission at each $k_\parallel$.

We can further characterize differences in the damping or emission as a function of scale, shown in Fig. 5. While qualitatively having similar structure, namely, increased resonant coupling as scales reach $|k|d_p \sim 1$, the details of the VDF lead to significant differences in the predicted wave emission and absorption, quantified as $\frac{\gamma_{Obs} - \gamma_{C\&B}}{|\gamma_{Obs} + \gamma_{C\&B}|}$. The differences in the parallel ion cyclotron branch agree with the parallel

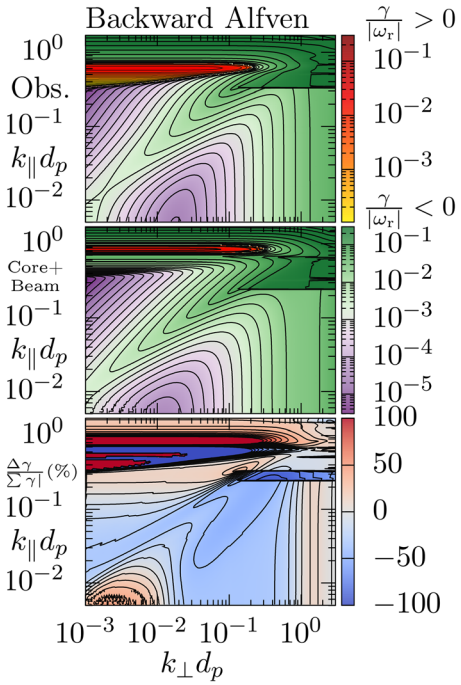

FIG. 5. Damping and growth rates for f_{Obs} (top) and $f_{C\&B}$ (middle) for the backwards propagating Alfvén wave solution. The percent difference between the two models is shown in the bottom panel, highlighting significant reductions in the kinetic Alfvén wave damping rates and increase in the ion cyclotron wave emission rates for the observed VDF compared to the bi-Maxwellian representation.

cut illustrated in Fig. 4. For $k_\perp d_p \lesssim 1$, the Alfvén wave transitions to a kinetic Alfvén wave, becoming strongly damped for both cases. However, the observed VDF has a significantly reduced damping rate compared to the core-and-beam response; a similar result is found for the forward solution. Such changes in the damping rates may impact the overall heating rates used in a variety of models for hot, weakly collisional systems,[35–38] that use bi-Maxwellian models for the determination of γ to inform the bifurcation of energy between ions and electrons.

V. CONTINUITY OF SOLUTIONS

To characterize the continuity between the observed and core-and-beam solutions, we determine dispersion relations associated with an ensemble of intermediate VDFs between the two models. At each point of the velocity grid, we calculate $\Delta f \equiv f_{Obs.} - f_{C\&B}$, and then construct N VDFs that continuously vary between the models as

$$f_i(v_\perp, v_\parallel) = f_{Obs.}(v_\perp, v_\parallel) + \frac{i\Delta f(v_\perp, v_\parallel)}{N-1}, \tag{25}$$

for $i \in [1, N]$. We then evaluate the ALPS solutions for all f_i and show the transition of the solutions between models based on $f_{Obs.}$ and $f_{C\&B}$. For this work, $N = 10$ elements are sufficient to smoothly track the change in the mode characteristics.

The normal mode structure in complex frequency space for the solutions associated with the full ensemble of VDFs at a fixed $(k_\perp, k_\parallel)d_p = (0.001, 0.0025)$ is illustrated in Fig. 6. The solutions

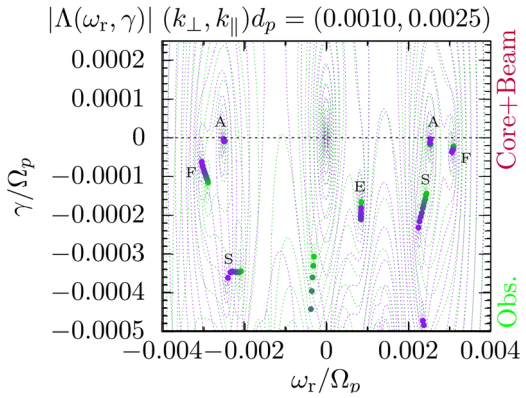

FIG. 6. Isocontours for constant values of the dispersion surface $\Lambda(\omega_r, \gamma)$ for ALPS solutions using $f_{Obs.}$ (green lines) and $f_{C\&B}$ (purple) at constant wavevector $(k_\perp, k_\parallel)d_p = (0.001, 0.0025)$. Identified Slow, Alfvén, Fast and Entropy solutions satisfying $\Lambda = 0$ are shown with dots. The continuity between the $f_{Obs.}$ and $f_{C\&B}$ solutions are shown with the intermediate f_i solutions, indicated by color.

from the intermediate VDFs produce a continuous path between the solutions based on the core-and-beam fit (purple) and the observed representation (green), indicating that ALPS produces solutions that smoothly vary between the models. At the selected wavevector, ω_r remains relatively unchanged for all f_i. For the damping rates, some of the solutions are qualitatively unaffected at this wavevector, e.g., both Alfvén solutions and the forward fast mode, by the variation in the underlying VDF. The compressive slow and entropy modes, as well as the backwards fast mode, undergo significant changes in their damping rates when transitioning from $f_{Obs.}$ to $f_{C\&B}$. There is not a universal increase or decrease in the damping rates when transitioning between the two models, but rather each mode responds uniquely to the variation, e.g., the backwards fast mode becomes more damped and the forwards slow mode becomes less damped for the observed VDF.

We next turn to a consideration of the variations of these solutions with wavevector, in particular, determining the impacts of the observed distribution on the wave's eigenfunction characteristics. In Fig. 7, we plot the real and imaginary parts of ω for the backwards and forwards Alfvén waves. The strong damping due to the proton cyclotron resonance acts to slow, and eventually reverse, the propagation direction of the forwards Alfvén solutions near $k_\parallel d_p \sim 1$. For the backwards solution, ω_r is qualitatively the same across $k_\parallel$ for all VDFs f_i from the ensemble. The perpendicular electric field polarization $\mathscr{P}_{xy}$ of the waves is constant across all evaluations, but the correlation between the density and the parallel magnetic field fluctuations

$$C(\delta n_p, \delta B_\parallel) = Re\left(\frac{\delta n_p \delta B_\parallel^*}{|\delta n_p||\delta B_\parallel|}\right), \tag{26}$$

is altered, with the amplitude of $C(\delta n_p, \delta B_\parallel)|$ increasing at large scales for the more observation-like VDFs (i.e., for low i). Given that such eigenfunction relations are frequently invoked as a means of identifying wave modes in space plasmas,[39–41] these changes in the eigenfunctions impact some interpretations of what waves are present in magnetospheric and solar wind plasmas.

The behavior of the fast and slow magnetosonic modes is also impacted by the velocity space structure. In Fig. 8, we plot the

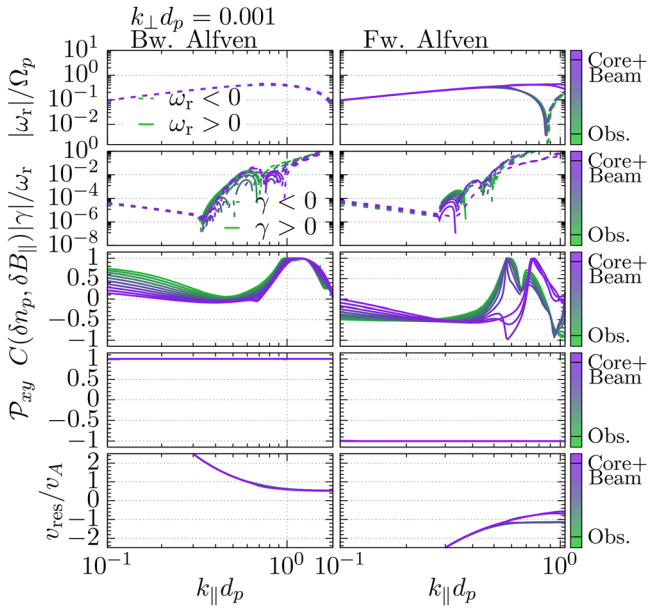

FIG. 7. Real part of the frequency ω_r/Ω_p, damping (dashed lines) and growth (solid) rates γ/ω_r, the density-B_z correlation, electric field polarization $\boldsymbol{P}_{xy}$, and v_{res} as a function of $k_\parallel d_p$ for fixed $k_\perp d_p$ for the forward and backward Alfvén solutions using the continuous set of VDFs.

dispersion relations for the forward parallel-propagating fast and slow solutions for the observed, core-and-beam, and intermediate VDFs. The forward fast and slow modes undergo a mode conversion, transitioning between the observed and fit distributions, similar to those seen near exceptional points.[42] The solution that is more weakly damped at MHD scales has a greater phase speed and a positive correlation between δn_p and $\delta B_\parallel$ when using the core-and-beam VDF. It remains the fastest, most weakly damped, and positive-C solution at smaller parallel wavevectors. The slower mode at MHD scales similarly remains more strongly damped and negatively correlated in C as the solution approaches $k_\parallel d_p \sim 1$.

However, when using the observed VDF, the faster and slower solutions at large scales exchange their phase speeds and senses of correlation between δn_p and $\delta B_\parallel$ at smaller scales, with the "slow" MHD mode becoming faster than the "fast" MHD mode. This change in the mode behavior is driven by a change in the correlation between the density and magnetic field fluctuations, shown in the right panel of Fig. 8. When using the core-and-beam model, the fast mode phase speed is enhanced by the in-phase response of δn_p and $\delta B_\parallel$, while the slow mode phase speed is lessened by its out-of-phase response. When using the observed VDF, these phase changes occur for the two modes around $k_\parallel d_p \sim 0.1$. By investigating the phases for the models using the intermediate VDF representations, we see that this exchange is not a numerical artifact, but is a smooth transition between the calculations with $f_{Obs.}$ and $f_{C\&B}$. Such variations in the correlation in plasmas with non-bi-Maxwellian background VDFs may impact the characterization of mode composition,[40,41] as well as the nonlinear coupling and participation in the turbulence cascade of compressible solutions[43,44] and warrant further study.

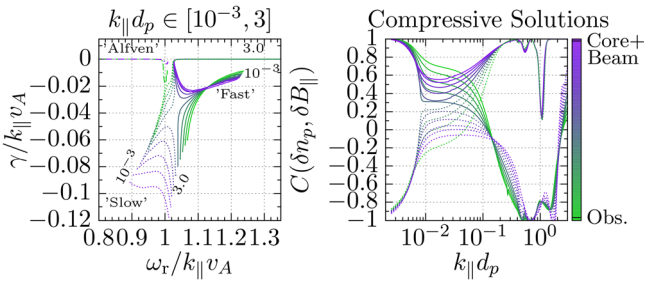

FIG. 8. Dispersion relations for the forward propagating fast and slow magnetoacoustic modes for the core-and-beam VDF $f_{C\&B}$, the observed VDF $f_{Obs.}$, and intermediate VDF representations f_i. (Left panel) Parametric curves of $[\omega_r, \gamma](k_\parallel, d_p)$ show distinct connections between the MHD-scale and ion-scale solutions for the observed and core-and-beam models. (Right) Variation in $C(\delta n_p, \delta B_\parallel)$ of the fast and slow solutions as a function of parallel wavevector.

VI. CONCLUSIONS

We have extended the Arbitrary Linear Plasma Solver (ALPS) by introducing a robust hybrid analytic continuation framework using high-order polynomial (Chebyshev) representations of arbitrary velocity distribution functions (VDFs) to determine the associated dielectric plasma response. The new Chebyshev generalized linear least squares (GLLS) approach delivers smooth and accurate continuations of the dispersion relation solutions to the linear Vlasov–Maxwell equations across $\gamma = 0$, eliminating discontinuities associated with low-order analytical fits and enabling reliable tracking of normal modes from unstable to damped regimes.

Through systematic comparisons between spacecraft-observed solar-wind proton VDFs and their best-fit two-component bi-Maxwellian representations, we demonstrate that the updated ALPS produces continuous solutions to the plasma dispersion relation between bi-Maxwellian and arbitrary VDF inputs. We find that mode polarizations and heating rates can vary significantly when accounting for non-(bi-)Maxwellian structure in the VDF, impacting interpretations of Alfvén, fast, and slow modes.

These advancements extend ALPS's applicability to a broad range of plasma environments such as the solar wind, magnetosheath, and astrophysical systems, where deviations from Maxwellian equilibria govern wave behavior and heating processes. By coupling numerical integration for arbitrary components with efficient bi-Maxwellian and cold-plasma models for fluid-like species, the updated hybrid solver offers improvements in computational speed. We anticipate that the improved analytic continuation and eigenfunction outputs will enable improved theoretical predictions and guide the interpretation of *in situ* spacecraft measurements in future studies.

ACKNOWLEDGMENTS

The authors thank the UCL Open Source Software Sustainability Project for their assistance in publishing ALPS as an open source code. This study benefited from support by the International Space Science Institute (ISSI) in Bern, through ISSI International Team project 24-612 ("Excitation and dissipation of kinetic-scale fluctuations in space plasmas"). K.G.K. was supported in part by Grant No. NSF PHY-2309135 to the Kavli Institute for Theoretical Physics (KITP) and NASA Grant Nos. 80NSSC19K0912 and 80NSSC24K0171. D.V. is supported by STFC Consolidated Grant No. ST/W001004/1.

AUTHOR DECLARATIONS

Conflict of Interest

The authors have no conflicts to disclose.

Author Contributions

K. G. Klein: Conceptualization (equal); Funding acquisition (equal); Software (equal); Visualization (lead); Writing – original draft (lead); Writing – review & editing (equal). **D. Verscharen:** Conceptualization (equal); Funding acquisition (equal); Software (equal); Writing – review & editing (equal).

DATA AVAILABILITY

The data that support the findings of this study are openly available at the ALPS repository at https://github.com/danielver02/ALPS, Ref. 48 with a full tutorial at https://danielver02.github.io/ALPS/, Ref. 13.

APPENDIX A: USING BI-MAXWELLIAN AND COLD PLASMA MODELS FOR SELECT SPECIES

For numerical expediency, ALPS has been updated to allow users to declare the susceptibility for any given component $\underline{\underline{\chi}}_s$ to be calculated using the numerical integration or using a bi-Maxwellian or cold plasma model. In all cases, ALPS solves Eq. (6), but with different representations of $\underline{\underline{\chi}}_s$. For the bi-Maxwellian case, we use the susceptibility as evaluated from NHDS,[8] which follows the notation by Stix.[22] The bi-Maxwellian susceptibility is given by

$$\underline{\underline{\chi}}_s = \hat{\boldsymbol{e}}_\parallel \hat{\boldsymbol{e}}_\parallel \frac{2\omega_{p,s}^2 U_s}{\omega k_\parallel w_{\perp s}^2} + \frac{\omega_{p,s}^2}{\omega} \sum_{n=-\infty}^{\infty} e^{-\lambda} \underline{\underline{Y}}_{n,s}, \tag{A1}$$

where

$$\underline{\underline{Y}}_{n,s} = \begin{pmatrix} \frac{n^2 I_n}{\lambda} A_n & -in(I_n - I_n') A_n & \frac{k_\perp}{\Omega_s} \frac{n I_n}{\lambda} B_n \\ in(I_n - I_n') A_n & \left(\frac{n^2}{\lambda} I_n + 2\lambda I_n - 2\lambda I_n'\right) A_n & \frac{ik_\perp}{\Omega_s}(I_n - I_n') B_n \\ \frac{k_\perp}{\Omega_j} \frac{n I_n}{\lambda} B_n & -\frac{ik_\perp}{\Omega_s}(I_n - I_n') B_n & \frac{2(\omega - n\Omega_s)}{k_\parallel w_{\perp s}^2} I_n B_n \end{pmatrix}, \tag{A2}$$

I_n is the modified Bessel function of order n with argument $\lambda = k_\perp^2 w_{\perp s}^2 / 2\Omega_s^2$,

$$A_n = \frac{1}{\omega} \frac{T_{\perp s} - T_{\parallel s}}{T_{\parallel s}} + \frac{1}{k_\parallel w_{\parallel s}} \frac{(\omega - k_\parallel U_s - n\Omega_s) T_{\perp s} + n\Omega_j T_{\parallel s}}{\omega T_{\parallel s}} Z_0, \tag{A3}$$

$$B_n = \frac{1}{\omega k_\parallel} (\omega - k_\parallel U_s) + \frac{\omega - n\Omega_j}{k_\parallel} A_n, \tag{A4}$$

$$Z_0(\zeta) = \frac{1}{\sqrt{\pi}} \mathscr{P} \int_{-\infty}^{\infty} dz \, \frac{e^{-z^2}}{z - \zeta} + i\sqrt{\pi}\, \mathrm{sgn}(k_\parallel) e^{-\zeta^2}, \tag{A5}$$

and $\zeta = (\omega - k_\parallel U_s - n\Omega_j)/k_\parallel w_{\parallel s}$.

For the cold plasma case, we use the cold plasma susceptibility accounting for field-aligned relative drifts between the species:[33]

$$\underline{\underline{\chi}}_s = \begin{pmatrix} S_s & -iD_s & J_s \\ iD_s & S_s & M_s \\ J_s & -M_s & P_s \end{pmatrix}, \tag{A6}$$

where $S_s = (R_s + L_s)/2$, $D_s = (R_s - L_s)/2$,

$$R_s = -\frac{\omega_{p,s}^2}{\omega^2} \frac{\omega - k_\parallel U_s}{\omega - k_\parallel U_s + \Omega_s}, \tag{A7}$$

$$L_s = -\frac{\omega_{p,s}^2}{\omega^2} \frac{\omega - k_\parallel U_s}{\omega - k_\parallel U_s - \Omega_s}, \tag{A8}$$

$$J_s = -\frac{\omega_{p,s}^2}{\omega^2} k_\perp U_s \frac{\omega - k_\parallel U_s}{(\omega - k_\parallel U_s)^2 - \Omega_s^2}, \tag{A9}$$

$$M_s = i\frac{\omega_{p,s}^2}{\omega^2} k_\perp U_s \frac{\Omega_s}{(\omega - k_\parallel U_s)^2 - \Omega_s^2}, \tag{A10}$$

and

$$P_s = -\frac{\omega_{p,s}^2}{\omega^2} \left[\frac{\omega^2}{(\omega - k_\parallel U_s)^2} + \frac{k_\perp^2 U_s^2}{(\omega - k_\parallel U_s)^2 - \Omega_s^2} \right]. \tag{A11}$$

Using the much more numerically efficient bi-Maxwellian or cold-plasma expressions, rather than direct integration of the momentum derivatives, this "hybrid approach" significantly decreases the computational costs, and is appropriate for cases in which some of the components are accurately treated as cold or a simple Maxwellian, e.g., in evaluating VDFs from hybrid plasma simulations or when some species are only known through their velocity moments rather than their full VDFs.

APPENDIX B: EIGENFUNCTIONS AND HEATING RATES

With the complex frequency ω determined, the eigenfunctions for the perturbed densities δn_s, velocities $\delta \boldsymbol{U}_s$, and electromagnetic fields $\boldsymbol{E}$ and $\boldsymbol{B}$ can be calculated through evaluation of the linearized Maxwell's equations, the continuity equation, and the wave equation Eq. (6), using the routines implemented in PLUME.[7] Time scales are normalized to the reference cyclotron frequency Ω_{ref} and spatial scales to the reference inertial length d_{ref}.

We choose the complex Fourier coefficient for $\hat{E}_x \equiv E_x/E_{\perp,1} = 1$, where $E_{\perp,1}$ is an arbitrary real constant used to specify the overall amplitude of the linear eigenfunction, and solve for the other components using Eq. (6) in terms of $E_{\perp,1}$, yielding

$$\hat{E}_\parallel \equiv \frac{E_\parallel}{E_{\perp,1}} = \frac{\Lambda_{yx}\Lambda_{zy} - \Lambda_{yy}\Lambda_{zx}}{\Lambda_{yy}\Lambda_{zz} - \Lambda_{yz}\Lambda_{zy}}, \tag{B1}$$

and

$$\hat{E}_{\perp,2} \equiv \frac{E_{\perp,2}}{E_{\perp,1}} = -\frac{\Lambda_{zx} + \Lambda_{zz}(E_\parallel/E_{\perp,1})}{\Lambda_{zy}} = \frac{\Lambda_{zx}\Lambda_{yz} - \Lambda_{zz}\Lambda_{yx}}{\Lambda_{yy}\Lambda_{zz} - \Lambda_{yz}\Lambda_{zy}}, \tag{B2}$$

where Λ_{ij} are the elements of the 3×3 tensor $\underline{\underline{\Lambda}}$ in Eq. (6).

Combining these solutions for the complex Fourier coefficients of the components of $\boldsymbol{E}$ with the solutions for the complex frequency ω and wavevector $\mathbf{k} = k_\perp \hat{\boldsymbol{x}} + k_\parallel \hat{\boldsymbol{z}}$, we find the complex Fourier coefficients of the magnetic field eigenfunctions using Faraday's Law, Fourier transformed in time and space, $\omega \boldsymbol{B} = c\mathbf{k} \times \boldsymbol{E}$, giving

$$\frac{B_{\perp,1}}{E_{\perp,1}} = -\frac{ck_{\parallel}(E_{\perp,2}/E_{\perp,1})}{\omega} = -\frac{k_{\parallel}d_{\rm ref}}{(v_A/c)(\omega/\Omega_{\rm ref})}\frac{E_{\perp,2}}{E_{\perp,1}}, \tag{B3}$$

$$\frac{B_{\perp,2}}{E_{\perp,1}} = \frac{ck_{\parallel} - ck_{\perp}(E_{\parallel}/E_{\perp,1})}{\omega} = -\frac{\left[k_{\perp}d_{\rm ref}(E_{\parallel}/E_{\perp,1}) - k_{\parallel}d_{\rm ref}\right]}{(v_A/c)(\omega/\Omega_{\rm ref})}, \tag{B4}$$

and

$$\frac{B_{\parallel}}{E_{\perp,1}} = \frac{ck_{\perp}(E_{\perp,2}/E_{\perp,1})}{\omega} = \frac{k_{\perp}d_{\rm ref}}{(v_A/c)(\omega/\Omega_{\rm ref})}\frac{E_{\perp,2}}{E_{\perp,1}}. \tag{B5}$$

We use the linearized continuity equation,

$$\frac{\partial \delta n_s}{\partial t} + U_s\frac{\partial \delta n_s}{\partial z} = -n_{0s}\nabla\cdot\delta\boldsymbol{U}_s, \tag{B6}$$

including the normalized equilibrium parallel flow U_s, which we can express in terms of the momentum drift for species s,

$$\overline{U}_s \equiv \frac{U_s}{v_{A,\rm ref}} = \frac{P_s}{m_{\rm ref}v_{A,\rm ref}}\frac{m_{\rm ref}}{m_s}, \tag{B7}$$

to solve for the complex Fourier coefficient of the normalized number density fluctuation, $\delta n_s/n_{0s}$, given by

$$\frac{\delta n_s}{n_{0s}} = \frac{k_{\perp}\delta U_{xs} + k_{\parallel}\delta U_{zs}}{\omega - k_{\parallel}U_s} = \frac{c}{v_{A,\rm ref}}\frac{k_{\perp}d_{\rm ref}(\delta\overline{U}_{xs}) + k_{\parallel}d_{\rm ref}(\delta\overline{U}_{zs})}{\omega/\Omega_{\rm ref} - k_{\parallel}d_{\rm ref}\overline{U}_s}\frac{E_{\perp,1}}{B_0}, \tag{B8}$$

where we normalize the velocity fluctuations as $\delta\overline{\boldsymbol{U}}_s = \delta\boldsymbol{U}_s/(cE_{\perp,1}/B_0)$.

We can then determine the perturbed velocity fluctuations for each component $\delta\boldsymbol{U}_s$ by recognizing that the total current density (including any parallel flow) due is $\mathbf{j}_s = q_s(n_{0s}\,\delta\boldsymbol{U}_s + \delta n_s U_s\hat{\boldsymbol{z}})$. Using the susceptibility tensor to calculate $\mathbf{j}_s$ through Eq. (1) yields

$$\delta\boldsymbol{U}_s = -\frac{i\omega}{4\pi q_s n_{0s}}\underline{\underline{\chi_s}}(\mathbf{k},\omega)\cdot\boldsymbol{E} - \frac{\delta n_s}{n_{0s}}U_s\hat{\boldsymbol{z}}, \tag{B9}$$

or

$$\delta\overline{U}_{x,s} = -\frac{i\omega}{\Omega_{\rm ref}}\left(\frac{v_{A,\rm ref}}{c}\right)^2\frac{n_{0,\rm ref}}{n_{0,s}}\frac{q_{\rm ref}}{q_s}\frac{\chi_{xl}E_l}{E_{\perp,1}},$$

$$\delta\overline{U}_{y,s} = -\frac{i\omega}{\Omega_{\rm ref}}\left(\frac{v_{A,\rm ref}}{c}\right)^2\frac{n_{0,\rm ref}}{n_{0,s}}\frac{q_{\rm ref}}{q_s}\frac{\chi_{yl}E_l}{E_{\perp,1}},$$

$$\delta\overline{U}_{z,s} = \frac{-\frac{i\omega}{\Omega_{\rm ref}}\left(\frac{v_{A,\rm ref}}{c}\right)^2\frac{n_{0,\rm ref}}{n_{0,s}}\frac{q_{\rm ref}}{q_s}\frac{\chi_{zl}E_l}{E_{\perp,1}} - \frac{k_{\perp}d_{\rm ref}\delta\overline{U}_{x,s}\overline{U}_s}{\omega/\Omega_{\rm ref} - k_{\parallel}d_{\rm ref}\overline{U}_s}}{1 + \frac{k_{\parallel}d_{\rm ref}\overline{U}_s}{\omega/\Omega_{\rm ref} - k_{\parallel}d_{\rm ref}\overline{U}_s}}. \tag{B10}$$

We compute the power emitted or absorbed by each component in the weak damping limit, following the routines implemented in PLUME,[7] which follow Stix,[22]

$$\frac{\gamma_s(\mathbf{k})}{\omega_{\rm r}(\mathbf{k})} = \boldsymbol{E}^*(\mathbf{k})\cdot\frac{\underline{\underline{\chi_s^a}}(\mathbf{k})\cdot\boldsymbol{E}(\mathbf{k})}{4W_{\rm EM}(\mathbf{k})}, \tag{B11}$$

where $\underline{\underline{\chi}}s^a(\mathbf{k})$ represents the anti-Hermitian component of the susceptibility for species s evaluated at $\gamma = 0$, $\boldsymbol{E}^*$ represents the complex conjugate of the fluctuating electric field, and

$$W_{\rm EM} = \boldsymbol{B}^*(\mathbf{k})\cdot\boldsymbol{B}(\mathbf{k}) + \boldsymbol{E}^*(\mathbf{k})\cdot\frac{\partial}{\partial\omega}[\omega\varepsilon_h(\mathbf{k})]\cdot\boldsymbol{E}(\mathbf{k}), \tag{B12}$$

is the electromagnetic wave energy, where ε_h is the Hermitian part of the dielectric tensor.

ALPS additionally decomposes the damping governed by the resonance condition $\omega - k_{\parallel}v_{\parallel} - n\Omega_s = 0$ into Landau Damping (LD), Transit Time Damping (TTD), and Cyclotron Damping (CD), following the prescription by Huang *et al.*[45] The $n = 0$ Landau resonance includes both LD, coupling $E_{\parallel}$ to a particle's charge,

$$P_s^{LD} = \frac{i\omega}{16\pi}\left[(\chi_{zz,s}^{(n=0)} - \chi_{zz,s}^{(n=0)*})E_zE_z^* + \chi_{zy,s}^{(n=0)}E_yE_z^* - \chi_{zy,s}^{(n=0)*}E_y^*E_z)\right]_{\omega=\omega_{\rm r}}, \tag{B13}$$

and TTD, coupling the magnetic field magnitude gradient $\delta B_{\parallel}$ to the magnetic moment via

$$P_s^{TTD} = \frac{i\omega}{16\pi}\left[(\chi_{yy,s}^{(n=0)} - \chi_{yy,s}^{(n=0)*})E_yE_y^* + \chi_{yz,s}^{(n=0)}E_yE_z^* - \chi_{yz,s}^{(n=0)*}E_y^*E_z)\right]_{\omega=\omega_{\rm r}}. \tag{B14}$$

In this context, $\chi_{ij}^{n=0}$ is the ijth susceptibility component evaluated for only $n = 0$.

CD occurs via $n \neq 0$ resonances due to forces by $E_{\perp}$ on the charged particles. The power absorption due to CD of the $n^{\rm th}$ harmonic is

$$P_s^{\rm CD,n} = \frac{\omega}{8\pi}\Big[|E_x|^2\left(\chi_{xx,s}^n - \chi_{xx,s}^{n,*}\right) + |E_y|^2\left(\chi_{yy,s}^n - \chi_{yy,s}^{n,*}\right) + \left(E_x^*E_y - E_y^*E_x\right)\left(\chi_{xy,s}^n - \chi_{yx,s}^{n,*}\right)\Big]_{\omega=\omega_{\rm r}}. \tag{B15}$$

As currently implemented, ALPS only outputs the CD power absorption/emission associated with the $n = \pm 1$ resonance.

APPENDIX C: THE LIMITS OF ANALYTIC CONTINUATION

Given the novel GLLS representation for the analytic continuation, it is important to quantify how far into imaginary parallel momentum space the representation can be accurately and reliably extended. Toward this end, we consider the continuations of three VDFs: a single Maxwellian, the best-fit core-and-beam bi-Maxwellian $f_{C\&B}(p_{\perp} = 0)$ used in Sec. IV A, and the observed VDF $f_{Obs.}(p_{\perp} = 0)$ is also described in Sec. IV A. We evaluate the amplitude of the complex-valued representation of the VDF $|f_p[\mathbb{R}e(p_{\parallel}), \mathbb{I}m(p_{\parallel}); p_{\perp} = 0]$ for all three models. For the GLLS representation, we apply orders 5, 10, 30, and 50. These comparisons are shown in Fig. 9, and the coefficients for the GLLS fits are shown in Fig. 10.

All orders of the GLLS method yield the quantitatively identical continuation behavior as the single Maxwellian representation when the underlying VDF is a single Maxwellian. This can be understood by noting that only two of the coefficients, a_0 and a_2, are effectively non-zero for all orders, blue lines in Fig. 10, regardless of the order of the GLLS representation. This matches our intuitive expectations, as the log of a Maxwellian is a second-order polynomial. This simple quadratic expression matches the single Maxwellian well, and the lack of additional terms in the

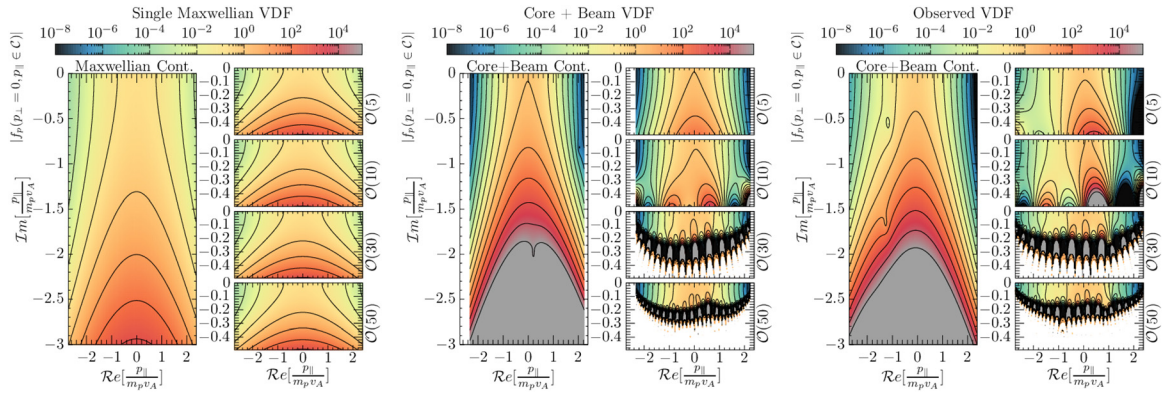

FIG. 9. The amplitude of $|f_p|$ evaluated at complex parallel momentum for $p_\perp = 0$ using one or two bi-Maxwellians, as well as for several orders of GLLS (5 through 50; right). The input VDFs are: (left) a single Maxwellian, (center) the core-and-beam bi-Maxwellian from Sec. IV A, and (right) the observed distribution from Sec. IV A.

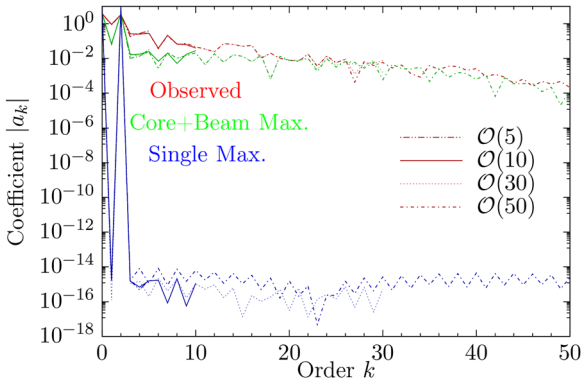

FIG. 10. Magnitude of coefficients of GLLS fits a_k for the three VDFs illustrated in Fig. 9.

representation produces the same complex structure at larger values of $|\mathbb{I}m(p_\parallel)|$.

For the core-and-beam VDF, a broader range of orders has non-negligible power. These additional terms lead to oscillations in the complex GLLS representation of f_p, and thus increased amplitudes of $|f_p|$, at larger $|\mathbb{I}m(p_\parallel)|$ values compared to the relatively shallower increase in $|f_p|$ when evaluating the sum of two Maxwellians in $f_{C\&B}$. This trend is further exacerbated for the observed distribution $f_{Obs.}$, where the non-Maxwellian structure in the VDF leads to more power in the lower-order coefficients a_k compared to either of the simpler VDFs.

This increase in $|f_p|$ impacts the resolution of strongly damped waves, as the associated values of $|\mathbb{I}m(p_\parallel)|$ for such modes are large enough for the numerical evaluation of the analytic continuation of f_p to be inaccurate. As seen in the right-hand panels of Fig. 9, there is a larger increase in $|f_p|$ with higher order representations for more strongly damped solutions. For this reason, users should select the lowest order representation sufficient to capture the VDF structure. This approach not only optimizes the numerical efficiency of this scheme, but it also avoids using unnecessarily high orders, which may introduce numerical artifacts for strongly damped solutions. Overall, given the superior behavior of the GLLS method for weakly damped solutions, we find that using the Chebyshev polynomials rather than a low-order Maxwellian fit is the optimal choice for non-Maxwellian VDFs.

REFERENCES

[1]S. P. Gary, *Theory of Space Plasma Microinstabilities* (Cambridge University Press, Cambridge, UK, 1993).
[2]D. Verscharen, S. Bourouaine, B. D. G. Chandran, and B. A. Maruca, "A parallel-propagating Alfvénic ion-beam instability in the high-beta solar wind," Astrophys. J. **773**, 8 (2013).
[3]K. G. Klein, B. L. Alterman, M. L. Stevens, D. Vech, and J. C. Kasper, "Majority of solar wind intervals support ion-driven instabilities," Phys. Rev. Lett. **120**, 205102 (2018).
[4]K. G. Klein, J. L. Verniero, B. Alterman, S. Bale, A. Case, J. C. Kasper, K. Korreck, D. Larson, E. Lichko, R. Livi, M. McManus, M. Martinović, A. Rahmati, M. Stevens, and P. Whittlesey, "Inferred linear stability of parker solar probe observations using one- and two-component proton distributions," Astrophys. J. **909**, 7 (2021).
[5]M. D. McManus, K. G. Klein, S. D. Bale, T. A. Bowen, J. Huang, D. Larson, R. Livi, A. Rahmati, O. Romeo, J. Verniero, and P. Whittlesey, "Proton- and alpha-driven instabilities in an ion cyclotron wave event," Astrophys. J. **961**, 142 (2024).
[6]K. Roennmark, "Waves in homogeneous, anisotropic multicomponent plasmas (WHAMP)," Technical Report (1982).
[7]K. G. Klein, G. G. Howes, and C. R. Brown, "PLUME: Plasma in a linear uniform magnetized environment," Res. Notes AAS **9**, 102 (2025).
[8]D. Verscharen and B. D. G. Chandran, "NHDS: The new Hampshire dispersion relation solver," Res. Notes AAS **2**, 13 (2018).
[9]H.-S. Xie, "BO: A unified tool for plasma waves and instabilities analysis," Comput. Phys. Commun. **244**, 343–371 (2019).
[10]P. Astfalk, T. Görler, and F. Jenko, "DSHARK: A dispersion relation solver for obliquely propagating waves in bi-kappa-distributed plasmas," J. Geophys. Res. **120**, 7107–7120, https://doi.org/10.1002/2015JA021507 (2015).
[11]E. Marsch, "Helios: Evolution of distribution functions 0.3–1 AU," Space Sci. Rev. **172**, 23–39 (2012).
[12]D. Verscharen, K. G. Klein, and B. A. Maruca, "The multi-scale nature of the solar wind," Living Rev. Sol. Phys. **16**, 5 (2019).
[13]K. G. Klein, D. Verscharen, T. Koskela, and D. Stansby, see https://danielver02.github.io/ALPS/ "danielver02/alps: Zenodo Release" (ALPS, 2023).
[14]D. Verscharen, K. G. Klein, B. D. G. Chandran, M. L. Stevens, C. S. Salem, and S. D. Bale, "ALPS: The arbitrary linear plasma solver," J. Plasma Phys. **84**, 905840403 (2018), arXiv:1803.04697 [physics.space-ph].
[15]W. Jiang, D. Verscharen, H. Li, C. Wang, and K. G. Klein, "Whistler waves as a signature of converging magnetic holes in space plasmas," Astrophys. J. **935**, 169 (2022).

[16]W. Jiang, D. Verscharen, S.-Y. Jeong, H. Li, K. G. Klein, C. J. Owen, and C. Wang, "Velocity-space signatures of resonant energy transfer between whistler waves and electrons in the Earth's magnetosheath," Astrophys. J. **960**, 30 (2024).
[17]A. S. Afshari, G. G. Howes, J. R. Shuster, K. G. Klein, D. McGinnis, M. M. Martinović, S. A. Boardsen, C. R. Brown, R. Huang, D. P. Hartley, and C. A. Kletzing, "Direct observation of ion cyclotron damping of turbulence in Earth's magnetosheath plasma," Nat. Commun. **15**, 7870 (2024).
[18]J. Walters, K. G. Klein, E. Lichko, M. L. Stevens, D. Verscharen, and B. D. G. Chandran, "The effects of nonequilibrium velocity distributions on Alfvén ion-cyclotron waves in the solar wind," Astrophys. J. **955**, 97 (2023).
[19]M. F. Zhang, M. W. Kunz, J. Squire, and K. G. Klein, "Extreme heating of minor ions in imbalanced solar-wind turbulence," Astrophys. J. **979**, 121 (2025).
[20]A. Fitzmaurice, J. F. Drake, and M. Swisdak, "Ion beam instabilities during solar flare energy release," Phys. Plasmas **32**, 042114 (2025).
[21]D. L. Schröder, H. Fichtner, M. Lazar, D. Verscharen, and K. G. Klein, "Temperature anisotropy instabilities of solar wind electrons with regularized kappa-halos resolved with alps," Phys. Plasmas **32**, 032109 (2025).
[22]T. H. Stix, *Waves in Plasmas, by Stix, Thomas Howard; Stix, Thomas Howard* (American Institute of Physics, New York, 1992).
[23]K. G. Klein and B. D. G. Chandran, "Evolution of the proton velocity distribution due to stochastic heating in the near-Sun solar wind," Astrophys. J. **820**, 47 (2016).
[24]The relativistic case is more complex, given the non-trivial momentum dependence of the resonant denominator in that limit; see §3.3 by Verscharen:2018[14] for details, where we use the method suggested by Lerche:1967[46] to transform from $(p_\parallel, p_\perp)$ to $(\Gamma, \bar{p}_\parallel)$ and make the solution tractable.
[25]L. Landau, "On the vibrations of the electronic plasma," J. Phys. **10**, 25–34 (1946).
[26]B. L. Alterman, J. C. Kasper, M. L. Stevens, and A. Koval, "A comparison of alpha particle and proton beam differential flows in collisionally young solar wind," Astrophys. J. **864**, 112 (2018).
[27]K. Levenberg, "A method for the solution of certain non-linear problems in least squares," Q. Appl. Math. **2**, 164–168 (1944).
[28]D. W. Marquardt, "An algorithm for least-squares estimation of nonlinear parameters," J. Soc. Ind. Appl. Math. **11**, 431–441 (1963).
[29]W. H. Press, S. A. Teukolsky, W. T. Vetterling, and B. P. Flannery, *Numerical Recipes in C*, 2nd ed. (Cambridge University Press, 1992).
[30]J. Mason and D. Handscomb, *Chebyshev Polynomials* (CRC Press, 2002).
[31]We use relative percent difference rather than relative error as we are frequently evaluating the dispersion relation in the frame where the parallel velocity moment of the VDF under consideration is effectively zero.
[32]As we are focused on modeling thermal populations in the solar wind, for the remainder of the manuscript we consider $f_{0,s}$ as a function of velocity rather than momentum.
[33]D. Verscharen and B. D. G. Chandran, "The dispersion relations and instability thresholds of oblique plasma modes in the presence of an ion beam," Astrophys. J. **764**, 88 (2013).
[34]C. F. Kennel and F. Engelmann, "Velocity space diffusion from weak plasma turbulence in a magnetic field," Phys. Fluids **9**, 2377–2388 (1966).
[35]G. G. Howes, "A prescription for the turbulent heating of astrophysical plasmas," Mon. Not. R. Astron. Soc. **409**, L104–L108 (2010).
[36]A. Chael, M. Rowan, R. Narayan, M. Johnson, and L. Sironi, "The role of electron heating physics in images and variability of the Galactic Centre black hole Sagittarius A," Mon. Not. R. Astron. Soc. **478**, 5209–5229 (2018).
[37]W. Gorman and K. G. Klein, "Mind the gap: Non-local cascades and preferential heating in high-β Alfvénic turbulence," Mon. Not. R. Astron. Soc. **531**, L1–L7 (2024).
[38]N. Shankarappa, K. G. Klein, M. M. Martinović, and T. A. Bowen, "Estimated heating rates due to cyclotron damping of ion-scale waves observed by the parker solar probe," Astrophys. J. **973**, 20 (2024).
[39]D. Krauss-Varban, N. Omidi, and K. B. Quest, "Mode properties of low-frequency waves: Kinetic theory versus Hall-MHD," J. Geophys. Res. **99**, 5987–6009, https://doi.org/10.1029/93JA03202 (1994).
[40]K. G. Klein, G. G. Howes, J. M. TenBarge, S. D. Bale, C. H. K. Chen, and C. S. Salem, "Using synthetic spacecraft data to interpret compressible fluctuations in solar wind turbulence," Astrophys. J. **755**, 159 (2012).
[41]D. Verscharen, C. H. K. Chen, and R. T. Wicks, "On kinetic slow modes, fluid slow modes, and pressure-balanced structures in the solar wind," Astrophys. J. **840**, 106 (2017).
[42]Exceptional points satisfy $\Lambda(\omega) = 0$ and $d_\omega\Lambda(\omega) = 0$ and act as branch points that allow continuous variations in the inputs to the dispersion relation to smoothly vary between different normal mode solutions; c.f. the Appendix of Klein:2015a.[47]
[43]A. A. Schekochihin, S. C. Cowley, W. Dorland, G. W. Hammett, G. G. Howes, E. Quataert, and T. Tatsuno, "Astrophysical gyrokinetics: Kinetic and fluid turbulent cascades in magnetized weakly collisional plasmas," Astrophys. J. Suppl. Ser. **182**, 310–377 (2009).
[44]Y. Kawazura, A. A. Schekochihin, M. Barnes, J. M. TenBarge, Y. Tong, K. G. Klein, and W. Dorland, "Ion versus electron heating in compressively driven astrophysical gyrokinetic turbulence," Phys. Rev. X **10**, 041050 (2020).
[45]R. Huang, G. G. Howes, and A. J. McCubbin, "The velocity-space signature of transit-time damping," J. Plasma Phys. **90**, 535900401 (2024).
[46]I. Lerche, "Unstable magnetosonic waves in a relativistic plasma," Astrophys. J. **147**, 689 (1967).
[47]K. G. Klein and G. G. Howes, "Predicted impacts of proton temperature anisotropy on solar wind turbulence," Phys. Plasmas **22**, 032903 (2015).
[48]See https://github.com/danielver02/ALPS for the repository for "ALPS."